J MATER SCI 41 (2006) 779–792

Defect structure in GaN pyramids

JEFFREY K. FARRER
Department of Physics and Astronomy, Brigham Young University, Provo, UT 84602

C. BARRY CARTER
Department of Ch. E. & Materials Science, University of Minnesota, Minneapolis, MN 55455

High-quality GaN/AlN layers grown on (111) Si substrates have been used as the seeding layer for lateral epitactic overgrowth of GaN. The selective overgrowth was controlled by depositing a Si_3N_4 mask on the GaN seed layer. Growth of additional GaN resulted in the formation of GaN pyramids above the apertures in the patterned Si_3N_4 mask. Transmission electron microscopy showed that the GaN pyramids, the GaN seed layer, and the AlN buffer layer in the samples have the following epitactic relationship with respect to the silicon substrate: $[11\bar{2}0]_{GaN}||[11\bar{2}0]_{AlN}||[\bar{1}10]_{Si}$ and $(0001)_{GaN}||(0001)_{AlN}||(111)_{Si}$. The pyramids were found to consist of a defective core region and a nearly defect-free outer region. In the core of the pyramid (at, or above, the aperture in the mask), numerous dislocations thread through the pyramid perpendicular to the interface plane. Some of these threading dislocations, which originated from the GaN/AlN seed layer, bend abruptly through 90° at the edge of this core region. In the outer part of the GaN pyramid, the density of vertically propagating dislocations was much lower. Most of the dislocations in this region are closely parallel to the original (0001) substrate plane. The top few microns of material are found to be essentially defect-free. The growth mechanism of the GaN pyramids is discussed in light of this defect structure.
© *2006 Springer Science + Business Media, Inc.*

1. Introduction

Due to their wide direct bandgap and good thermal, chemical, and mechanical stability III–V nitrides have been extensively investigated for use in microelectronic and optoelectronic devices [1–5]. The performance of these devices is often directly related to the type (i.e. Burgers vector) and density of dislocations present in the materials used in the device. Lateral epitactic overgrowth (LEO) is a technique for producing heteroepitactic GaN films which have a low defect density [6–14]. In LEO, epitactic growth is initiated at seeds (apertures) in partially masked substrates. The substrates are usually lithographically patterned with an amorphous layer such as Si_2O or Si_3N_4. The lateral overgrowth occurs without competing nucleation on the masked areas, thus propagation of dislocations from the seeding layer is partially blocked by the mask [15]. LEO has been used for many years on a variety of different materials [16]; examples of its use include the reduction of dislocation densities in heteroepitactic semiconductor films of GaAs [17, 18] and the formation of grain boundaries in GaAs [19]. Subsequent work on laterally overgrown InP on InP-coated Si substrates indicated that LEO could be used to relieve stress caused by both the lattice mismatch and the difference in thermal expansion coefficient [20]. LEO is already used in the fabrication of field-effect transistors (FETs) [21, 22] and such semiconductor microstructures as quantum wires and quantum dots [23–26].

LEO of GaN on sapphire and SiC substrates has been reported [2, 6, 8, 9, 27–36], and reports of the growth of GaN on (111) Si have also been given [7, 37–46]. Studies indicate that the LEO of GaN on pattern-masked substrates can reduce the dislocation density by four to six orders of magnitude [47]. Most of these studies have included the use of a low-temperature AlN or GaN buffer layer to act as a seeding layer in the mask aperture [34, 48]. It has been shown that using a buffer layer considerably improves the crystal quality of the GaN epilayers [39, 49–53]. The selectively grown GaN structures presumably involve lateral epitaxy, i.e., epitactic growth parallel to, but not in contact with, the 0001 substrate surface. However, the relationship between the defect distribution and the growth mechanism is not fully understood.

Single-crystal Si wafers are particularly attractive as substrates for LEO due to their low cost, large size, and the potential for the integration of GaN-based optoelec-

0022-2461 © *2006 Springer Science + Business Media, Inc.*
DOI: 10.1007/s10853-006-6563-2

tronic devices with Si-based electronics. GaN heteroepitactic films grown on a Si substrate are expected to have higher dislocation densities than those grown on sapphire and SiC substrates. This difference is attributed to the larger lattice mismatch between Si and GaN. Using LEO, the high density of dislocations in the GaN seeding layer is not so important because only a small fraction of the defects propagate into the lateral-overgrowth material. It is possible to produce high-quality GaN material for devices using LEO on a Si substrate [7] (laser action in this material has been observed at room temperature [43, 54]).

At present, the understanding of the nature and distribution of defects in GaN heteroepitactic films produced by LEO is limited, especially for those films grown on a Si substrate. In the present paper, the defect structure in GaN pyramids grown above apertures in a patterned Si_3N_4 mask on a (111) Si substrate by LEO is discussed. Microstructural characterization has been carried out by transmission electron microscopy (TEM) and electron backscatter diffraction (EBSD). In the TEM the thickness-fringe contrast technique and the weak-beam dark-field (WBDF) technique has been used [55, 56]. The lateral-growth mechanism is then discussed in terms of the observed defect structure.

2. Experimental details

The GaN growth was carried out in a low-pressure metal-organic chemical-vapor deposition (MOCVD) system. A (111) Si wafer was etched in HF:H_2O, rinsed and dried immediately before loading into the system. The system was evacuated before the pressure was regulated at 10 Torr with a constant H_2 flow. The susceptor was inductively heated to 1150°C and the Si wafer was baked at this temperature for 10 min in flowing H_2. The deposition for the AlN buffer layer was initiated by flowing triethylaluminum (TEA) and ammonia (NH_3) into the reactor. The AlN buffer layer was grown for 20 min, resulting in a buffer-layer thickness of 100 nm. The subsequent GaN layer was grown with triethylgallium (TEG) for 30 min, resulting in a thickness of about 200 nm. A 100-nm-thick masking layer of Si_3N_4 was then deposited using plasma-enhanced chemical-vapor deposition (PECVD). By combining photolithography and reactive-ion etching (RIE), arrays of nearly circular apertures, 5 μm in diameter and 20 μm apart (center-to-center), were formed. The wafer was then reloaded into the MOCVD system for the lateral overgrowth. The system pressure was set at 76 Torr. As soon as the susceptor temperature reached 1050°C, the growth was started by flowing ammonia and TEG into the reactor. The total time for the lateral overgrowth was 3 h.

The cross-sectional specimens were prepared using the usual 'sandwich' techniques: two pieces of the sample with similar orientation were glued face-to-face with epoxy (see e.g., [56]). The sample was then sliced normal to the interface plane. This cut was, in some cases, from the apex of the pyramid down through the center of the Si_3N_4 mask. In other regions, the cut was outside the aperture in the Si_3N_4 mask. After mechanically grinding and dimpling the sandwich to a thickness of ~10 μm, the specimen was further thinned to electron transparency by ion-beam milling. The specimens were then studied in a Philips CM30 TEM operating at 200 or 300 kV. The composition was analyzed using an Edax PV9900 XEDS (X-ray energy-dispersive spectrum) system attached to the TEM. The morphology of the as-grown structures was also studied by secondary electron imaging in a SEM.

Another growth sample was allowed to continue until the substrate was completely covered with GaN approximately 15 μm in thickness. In the case of this second sample the apertures were 2.5 μm in diameter and 5 μm apart (center-to-center). This particular sample was characterized at the surface using SEM imaging and electron backscatter diffraction (EBSD).

3. Results and observations

3.1. GaN pyramids

A secondary-electron image of the as-grown structures, shown in Fig. 1a, indicates that each pyramid has predominantly six facets. These facets are similar to those reported for pyramids grown on sapphire and SiC substrates [57, 58]. The width of the base and the height of the pyramids are both approximately 15 μm. Schematics of the pyramid structure are shown in Fig. 1b and c. Fig. 1b represents a top view of the pyramid, which shows the location of the aperture in the Si_3N_4 mask, above which the core region of the pyramid is grown. It also shows the lateral growth portion of the pyramid surrounding the core. The vertical bar indicates from approximately where in the pyramid the TEM cross-section sample (shown in Fig. 5) was taken. Fig. 1c is a schematic representing a cross-section view of the pyramid which shows the GaN/AlN seeding layer and the (111)Si substrate. The core region is shown containing vertical lines which represent the threading dislocations that start at the seed layer. The lateral growth region, outside the core, contains horizontal lines, which represent dislocations that run parallel to the growth interface.

Fig. 2 is a visible-light-microscope (VLM) image of the cross-sectional specimen. The pyramids can clearly be seen on either side of the glue line. The facet angles seen in the image vary because the sample has not been cut across one row of pyramids: it is at an angle to a particular row and cuts the pyramids at different heights and angles. Using a suitable polarizer VLM can reveal the interface between the pyramids and the substrate, and show some fine structure in the center of the pyramids. The height and width of the pyramids are determined to be ~15 μm from these images.

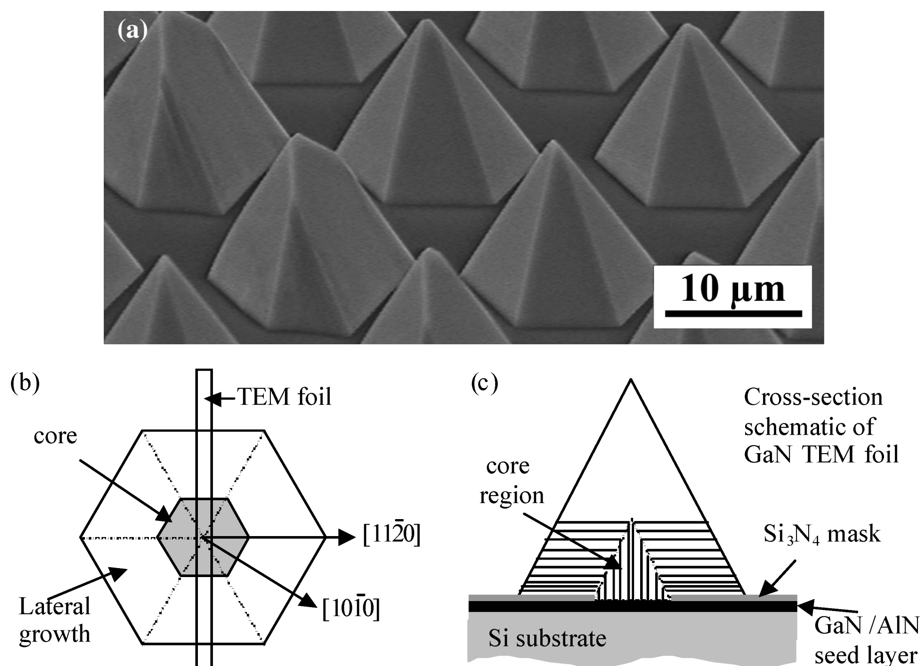

Figure 1 A secondary-electron SEM image of the as-grown GaN pyramids (a). Schematics representing a top view (b) and a cross section (c) of the pyramid structure.

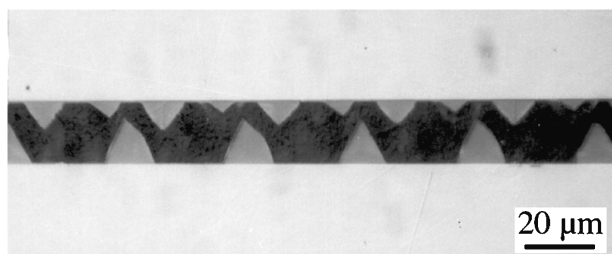

Figure 2 Visible-light-microscope (VLM) image of the cross-sectional specimen showing two arrays of pyramids being prepared for TEM. Apparent size depends on how the sample was sectioned.

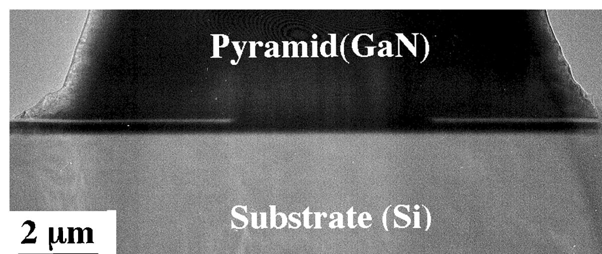

Figure 3 Mass contrast TEM image showing the window in the mask (light horizontal lines).

Fig. 3 is a low-magnification mass-thickness-contrast TEM image of the cross-sectional specimen. The mask (with a low average Z) is seen as a bright line between the pyramid and substrate. The thickness of the mask is ~80 nm. The size of the aperture in the mask is ~5 μm and the base size of the pyramid is 15 μm, consistent with the VLM observations. The GaN pyramids clearly extend laterally well beyond the aperture. The contrast in the image also suggests that there is a layer between the Si_3N_4 mask and the substrate. This region consists of two separate layers with thickness of 150 nm and 125 nm, respectively. From dark-field STEM images of the interface region and the corresponding X-ray composition maps for the elements Ga, Al, Si, and O, evidence was found for Al in the Si substrate which could be the result of Al diffusion into the Si substrate from the gas-phase Al precursor during the initial growth of the AlN buffer layer.

The crystallographic orientation of the different regions was obtained from selected-area diffraction (SAD) patterns. Fig. 4a is the SAD pattern from the entire interfacial region between the pyramid and substrate, (b) is the SAD pattern from the interface between the GaN plus AlN buffer layer and substrate, (c) is the SAD pattern from the GaN layer and AlN buffer layer, (d) is the SAD pattern from the substrate; and (e) is the SAD pattern from the GaN pyramid. The SAD patterns confirmed that the GaN pyramids, the GaN seed layer, and the AlN buffer layer are all monocrystalline with the following epitactic relationship with respect to the Si substrate:

$$[11\bar{2}0]_{\mathrm{GaN}}||[11\bar{2}0]_{\mathrm{AlN}}||[\bar{1}10]_{\mathrm{Si}}$$

$$(0001)_{\mathrm{GaN}}||(0001)_{\mathrm{AlN}}||(111)_{\mathrm{Si}}.$$

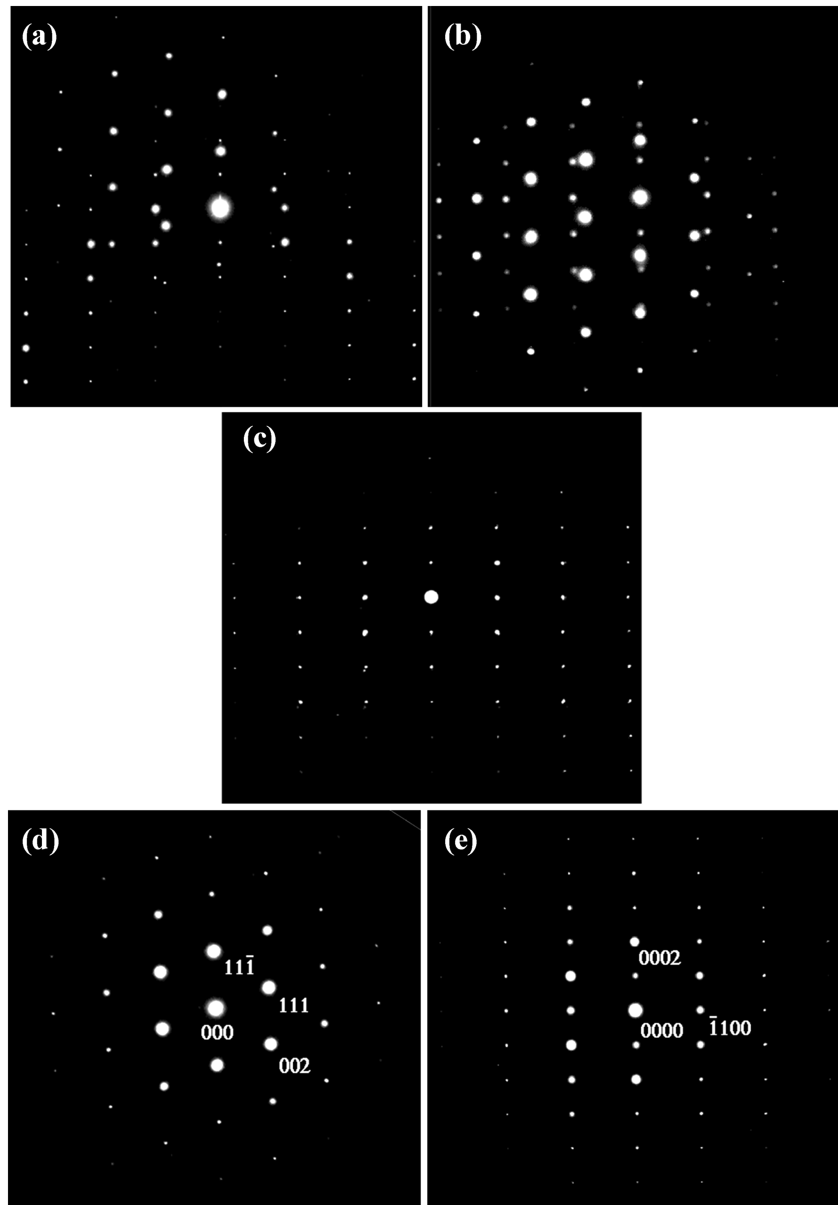

Figure 4 (a) SAD pattern from the whole interfacial region between the pyramid and the substrate, (b) SAD pattern from the interface between the GaN plus AlN buffer layer and substrate, (c) SAD pattern from the GaN layer and AlN buffer layer, (d) SAD pattern from the substrate whose zone axis is [$\bar{1}$10], and (e) SAD pattern from the GaN pyramid, the zone axis is [11$\bar{2}$0].

3.2. Dislocation geometry

Fig. 5 is a low-magnification weak-beam dark-field (WBDF) image of one of the GaN pyramids in cross section. The image was obtained with the electron beam nearly parallel to the [11$\bar{2}$0] GaN zone axis using a **g**(3**g**) weak-beam condition, **g** = [1$\bar{1}$00]. The ratio of the height to the half width of the base of the pyramid was ∼1.7, which is close to the c/a ratio for the wurtzite GaN. This aspect ratio is consistent with the six major inclined facets of each pyramid being parallel to {10$\bar{1}$1} planes. In the center of the GaN pyramid, at and above the aperture, dislocations propagate nearly perpendicular to the initial substrate plane and the dislocation density is quite high. In the outer part of the pyramid, the dislocations lie parallel to the interface plane. It is also apparent that the density of the defects in the outer part is lower than that in the core part of the pyramid. Since the width of the core region decreases with increasing distance from the interface plane, the overall defect density also decreases. Fig. 6 is a pair of DF images acquired under different diffraction conditions, which show that the top several microns of pyramid are essentially free of extended defects.

Fig. 7 is a WBDF image at a higher magnification than that of Fig. 5. The image was obtained with the electron beam nearly parallel to the [11$\bar{2}$0] GaN zone axis, and using a **g**(5**g**) condition, **g** = [0002]. This image re-

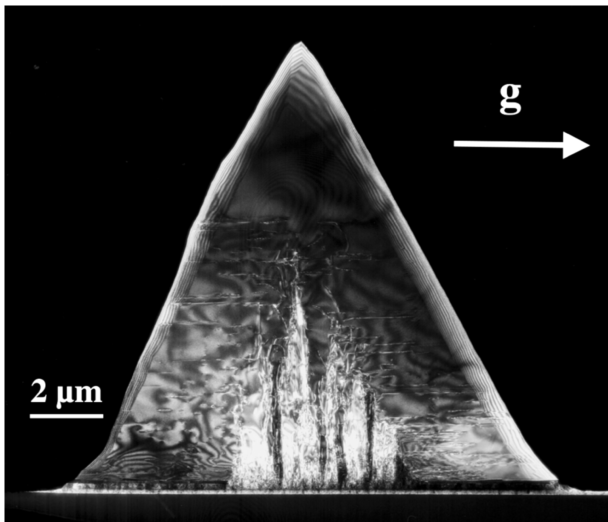

Figure 5 A low magnification TEM image of the cross-section specimen acquired under weak-beam, dark-field (WBDF) conditions.

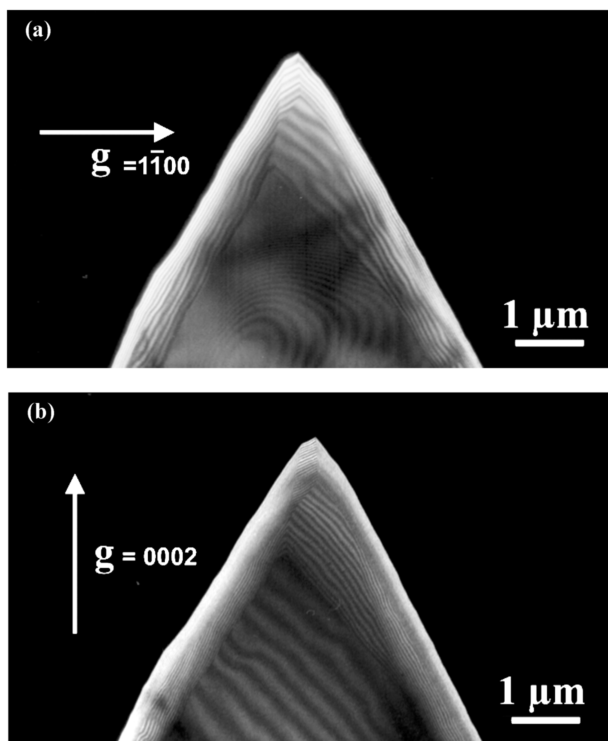

Figure 6 WBDF images of the top of a GaN pyramid. Images acquired near the $[11\bar{2}0]$ zone axis with $\mathbf{g} = 1\bar{1}00$ (a) and $\mathbf{g} = 0002$ (b). These images show that the top portion of the pyramid is essentially defect free.

veals the microstructure near the boundary of the core region of the pyramid. "M" refers to the Si_3N_4 mask, and "GA" refers to the GaN-seed layer with the AlN buffer layer. The dislocations can clearly be seen threading up through the core region and then turning abruptly, at the inclined boundary of the core, to lie parallel to the substrate. The location of the "bending" of the dislocations

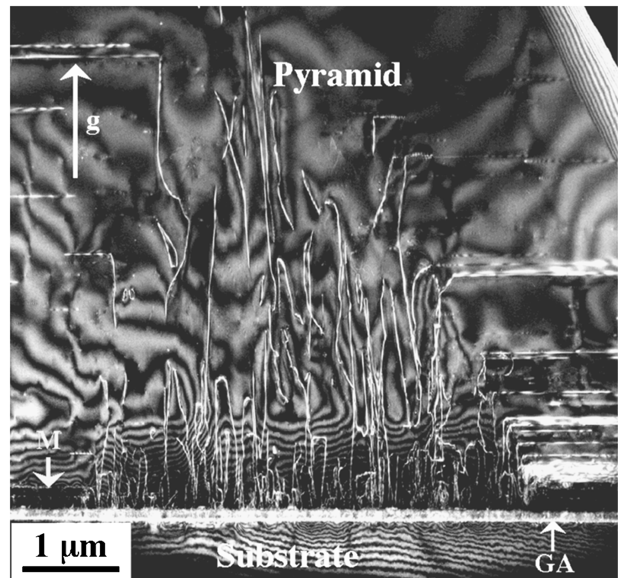

Figure 7 A WBDF image of the boundary of the core region of the pyramid. M refers to the Si_3N_4 mask, and "GA" refers to the GaN-seed layer with the AlN buffer layer.

indicates approximately where the lateral growth of the pyramid begins.

In the core region of the pyramid, the density of dislocations appears to be higher than any other region of the pyramid, and similar to that of an epitactically grown film of GaN not using the LEO technique [59]. It has been reported that the predominant defects in the core region are threading dislocations resulting from the misfit strain introduced by the lattice mismatch between the epilayer and substrate. The nature of these dislocations is reported to be mostly edge with $\mathbf{b} = 1/3\langle 11\bar{2}0\rangle$ [60–62].

3.3. Dislocation characterization

TEM studies have revealed that within a wurtzite GaN epilayer grown on a sapphire substrate, the dislocations are found mainly to have Burgers vectors $1/3\langle 11\bar{2}0\rangle$, $1/3\langle 11\bar{2}3\rangle$, and [0001] [59, 62]. This is in agreement with the fact that the wurzite structure is known to have the same possible perfect dislocations and slip systems as the *hcp* structure. Therefore, the dislocations with Burgers vectors of type $1/3\langle 11\bar{2}0\rangle$ lie on either the (0001) basal plane or the $\{1\bar{1}00\}$ prismatic planes. Dislocations of Burgers vector $1/3\langle 11\bar{2}3\rangle$ lie on the $\{10\bar{1}1\}$ pyramidal planes, and those with Burgers vector of [0001] lie on the $\{1\bar{1}00\}$ prismatic planes [63].

Fig. 8 is WBDF image acquired from the same area of the GaN pyramid as that shown in Fig. 7. The image in Fig. 8, however, was acquired with the electron beam near the $[10\bar{1}0]$ GaN zone axis, and using a $\mathbf{g}(3\mathbf{g})$ WB condition where $\mathbf{g} = [11\bar{2}0]$. The WBDF image in Fig. 7 was

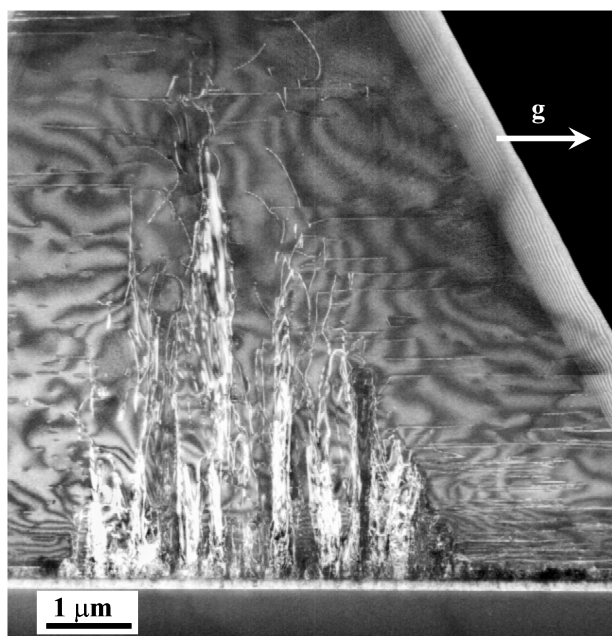

Figure 8 WBDF image of the same area as that found in Fig. 7. The image was acquired with the electron beam near the $[1\bar{1}00]$ GaN zone axis, and using a $\mathbf{g}(3\mathbf{g})$ WB condition where $\mathbf{g} = [11\bar{2}0]$.

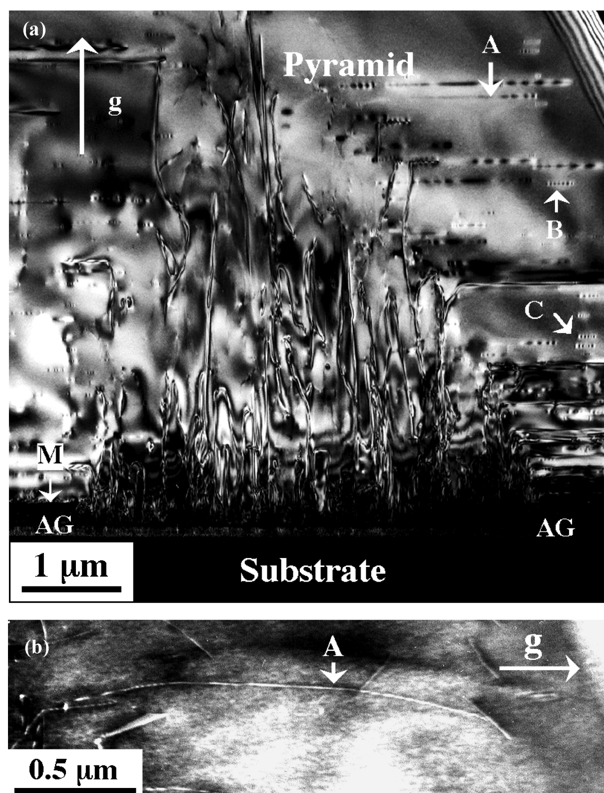

Figure 9 (a) DF image acquired near the $[11\bar{2}0]$ zone axis with $\mathbf{g} = 0002$ revealing the dislocation distribution in the core region (at the window) of a GaN pyramid. In the Figure, "M" indicates location of Si_3N_4 mask, "AG" indicates location of GaN seed layer and AlN buffer layer. (b) WBDF image of dislocation A with weak-beam condition $\mathbf{g}(6\mathbf{g})$, $\mathbf{g} = \bar{1}100$ (the electron beam is close to the $[11\bar{2}1]$ zone axis).

acquired with the electron beam near the $[11\bar{2}0]$ GaN zone axis, and using a $\mathbf{g}(5\mathbf{g})$ condition where $\mathbf{g} = [0002]$. By using different diffraction conditions to image the same area of one of the GaN pyramids, some general observations of the dislocations in the core region were made. First, it was apparent that there are more dislocations visible when $\mathbf{g} = [11\bar{2}0]$ than when $\mathbf{g} = [0002]$, which demonstrates that the density of the dislocations without a *c*-component to their Burgers vector is much higher than that of dislocations with a *c*-component. Furthermore, most of the dislocations observed under the diffraction conditions of Fig. 7, where the majority of dislocations are out of contrast, are actually dislocation half-loops which originate at the GaN/AlN seed layer. These observations are consistent with the expectations that the threading dislocations in the core region of Fig. 8 are mainly edge in nature and have either $1/3[11\bar{2}0]$-type or $1/3[11\bar{2}3]$-type Burgers vectors; and the half loops within the core region of Fig. 7 are either screw or mixed in nature and have Burgers vectors of type [0001].

Fig. 9 is another pair of DF images from the GaN pyramid. Fig. 9a, which was recorded with the electron beam tilted off the $[11\bar{2}0]$ GaN zone axis with $\mathbf{g} = 0002$, reveals some of the characteristics of the dislocations in the outer part of the pyramid. Specifically, the dislocations shown to be parallel to the original (0001) interface plane demonstrate an oscillatory intensity. This observation indicates that although the dislocations lie on the basal plane, they are also inclined to the foil surface. Using trace analysis [56], it can be confirmed that the line direction of most of the lateral dislocation shown in Fig. 9a, is close to the $[1\bar{1}00]$ direction, but it was found that several of these dislocation curve off of the $[1\bar{1}00]$ direction. Fig. 9b, which is a WBDF image recorded with the electron beam close to the $[11\bar{2}1]$ zone axis using a $\mathbf{g}(6\mathbf{g})$ condition where $\mathbf{g} = [1\bar{1}00]$, gives clear evidence that the dislocation labeled "A" curves from the core to the outer part of the pyramid, but remains parallel to the (0001) interface plane. The dislocations labeled "B" and "C" run through the thickness of the TEM foil, and again using trace analysis, the line direction of these dislocations was determined to be close to $[\bar{2}110]$. The two ends of these dislocations have been removed when thinning the TEM specimen. The contrast from these dislocations in Fig. 9a also suggests that the dislocations are either edge or mixed since a pure screw dislocation with its Burgers vector in the basal plane should be out of contrast since $\mathbf{g} \cdot \mathbf{b} = 0$ and $\mathbf{g} \cdot \mathbf{b} \times \mathbf{u} = 0$.

Evidence for dislocation climb during the growth is given in Fig. 10, which is a pair of WBDF images and corresponding schematics of a dislocation half-loop originating from the seeding layer. The images in Fig. 10a and c were acquired using $\mathbf{g} = 0002$ with a WBDF condition, the electron beam nearly parallel to $[11\bar{2}0]$ and $[01\bar{1}0]$, re-

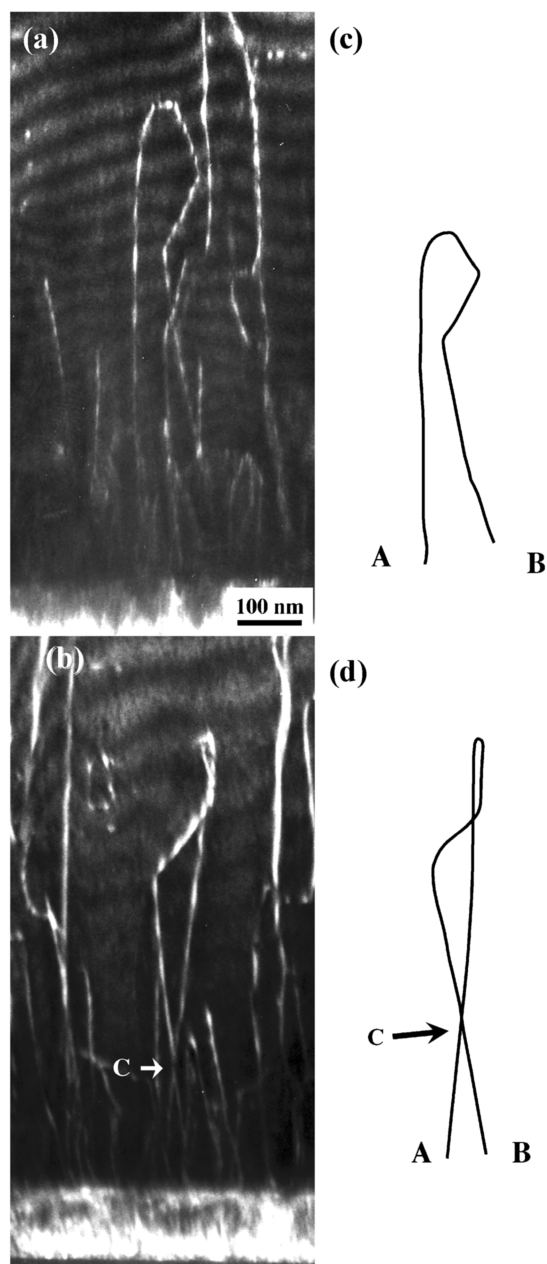

Figure 10 WBDF images of a dislocation half-loop originated from the seeding layer (a) $\mathbf{g} = 0002$ with $\mathbf{g}(9\mathbf{g})$ ([110] zone axis); (b) $\mathbf{g} = 0002$ with $\mathbf{g}(6\mathbf{g})$ ([010] zone axis). (c) and (d) are the schematics of the dislocation half-loop corresponding to (a) and (b), respectively. Point "C" in (b) represents the crossing point of the two ends of the half-loop.

spectively. Because the ends of this dislocation half-loop cross one another, as can be seen in the WBDF image of the tilted specimen in Fig. 10 (the crossing point is indicated by "C" in Fig. 10c), the two ends of this half-loop cannot lie in the same plane. These samples were not annealed after growth, so point defects must be incorporated during the growth process or while cooling. Thus, the half-loop propagates in the c-direction while absorbing point defects during growth or during subsequent cooling from the growth temperature.

TABLE I. A summary of the analysis from thickness fringes terminating at dislocations in Fig. 11

G	zone axis	A	B	C	D
$\mathbf{g} = 0\bar{1}13$	$[11\bar{2}1]$	0	0	−1	0
$\mathbf{g} = 000\bar{2}$	$[01\bar{1}0]$	0	0	0	0
$\mathbf{g} = 1\bar{1}0\bar{1}$	$[11\bar{2}0]$	−1	−1	0	−1
$\mathbf{g} = 1\bar{1}01$	$[11\bar{2}0]$	−1	−1	0	−1
Burgers vector		$1/3[\bar{2}110]$	$1/3[1\bar{2}10]$	$1/3[\bar{1}\bar{1}20]$	$1/3[1\bar{2}10]$
Line direction		$[2\bar{1}\bar{1}0]$	Loop	$[\bar{1}010]$	$[2\bar{1}\bar{1}0]$

3.4. Lateral dislocations

For further study of the dislocations that lie in the lateral growth regions, observations were made from cross-section TEM specimens that intersect the pyramid outside of the core region. The images shown in Fig. 11 are WBDF images of four defects (dislocations or dislocation loops) indicated as A, B, C, and D. The thickness fringes terminating at the ends of the dislocations can be used to determine the Burgers vectors of the dislocations using a thickness-fringe contrast analysis method [37, 55]. Both ends of all the dislocations can be seen clearly, however the thickness fringes which terminate on the left are used in the analysis. If the terminating fringe runs toward the top of the image, the number of fringes, n, is positive, otherwise n is negative. The number of fringes is then applied to the relation

$$n = \mathbf{g} \cdot \mathbf{b}$$

where $\mathbf{g}$ represents the diffracting vector. By selecting three diffracting vectors, $\mathbf{g}$, and determining n for each different condition, $\mathbf{b}$ can be unambiguously determined.

The results of the thickness-fringe analysis are summarized in Table I. A total of four different diffraction conditions are presented here although only three are needed for the Burgers vector analysis. The line directions of the dislocations, which are also reported in Table I, were obtained by trace analysis. From these results it has been determined that defect A is a screw dislocation, while defect B appears to be a dislocation half loop lying on the basal plane. Defects C and D are mixed dislocations; the character of these defects being that of 30° and 60° dislocations, respectively.

3.5. Electron Backscattered Diffraction (EBSD) of overgrown GaN pyramids

If the lateral growth is allowed to continue, the pyramids coalesce to become a continuous film covering the surface. Fig. 12 is a series of secondary electron images of the surface after the pyramids have grown together. The images were acquired at various sample tilts. The image in Fig. 12a was acquired at 0° sample tilt, so it is being viewed "flat." The images in Fig. 12b and c are tilted in opposite directions to show that the structures are actually pits. By viewing the film with transmitted light in a vis-

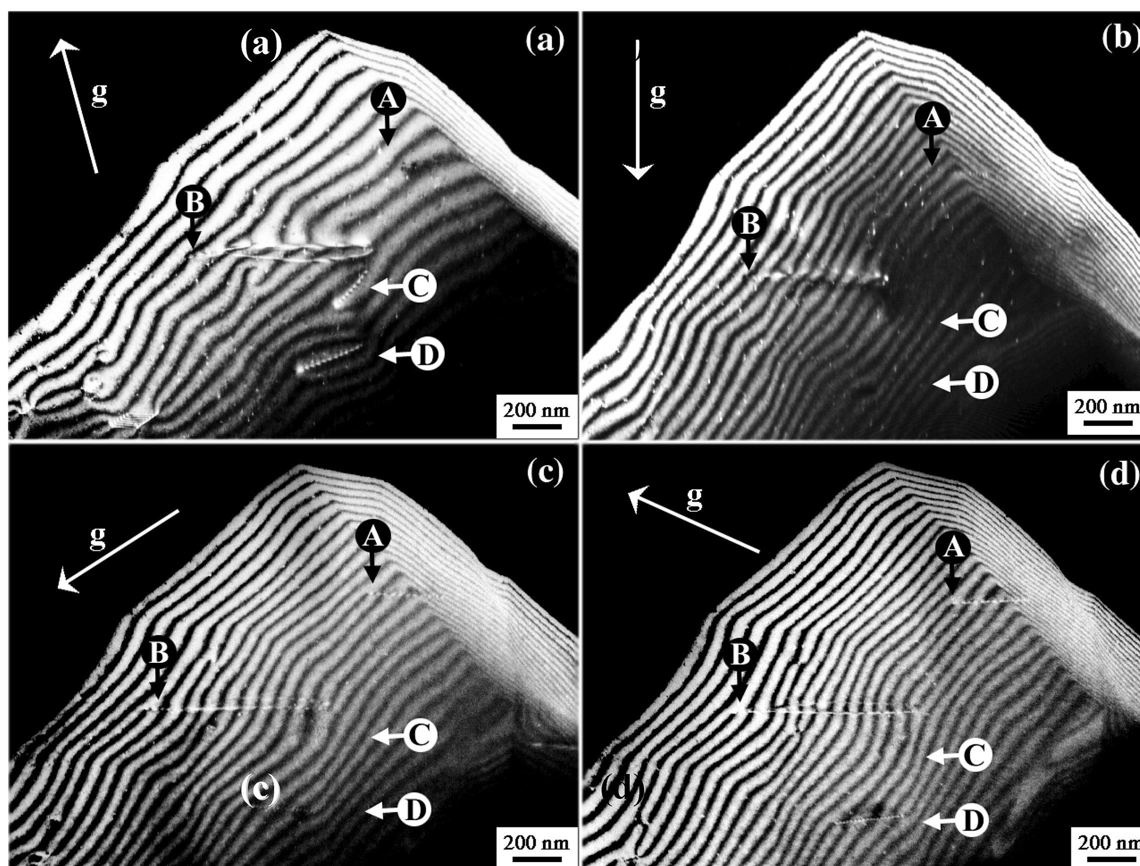

Figure 11 WBDF images of four different dislocations or dislocation loops labeled *A*, *B*, *C* and *D* in each image. The diffraction conditions are **g**(5**g**), with **g** equal to (a) $0\bar{1}13$, (b) 0002, (c) $[0\bar{1}0\bar{1}]$, and (d) $1\bar{1}01$.

ible light microscope it was determined that the growth aperture is located directly below the flat, plateau like structure. This structure is seen in Fig. 12a as having very dark contrast. Therefore, the pits are located at the triple junctions of three coalescing pyramids. From the images in Fig. 12 it can be seen that the pits have twelve facets whereas the pyramids, shown in Fig. 1, have only six.

EBSD was used to determine and map the orientations of the surface in order to detect the presence of any misorientations that may have resulted from the coalescence of the pyramids. Fig. 13a shows an EBSD pattern acquired from the surface of the overgrown GaN layer. By indexing this pattern the surface orientation was verified as the (0001) surface of GaN. Fig. 14a is an image quality (IQ) map, which is constructed using the quality (i.e. the brightness and contrast) of the EBSD patterns collected in 1 μm steps on the surface. In this case, the image quality (IQ) map gives an indication of the surface morphology due to variations at the surface. The IQ map also indicates the absence of grain boundaries at the surface. Grain boundaries normally appear as dark lines in an IQ map due to the poor quality of EBSD patterns that are acquired at the grain boundaries. The pits appear black in the IQ map due to the fact that no EBSD patterns are acquired from them.

It can be seen from Fig. 14a that the pits are arranged similarly to the arrangement seen in Fig. 12. The location of the original pyramid is roughly at the center of six pits, which form a hexagon around the location of the aperture in the Si_3N_4 mask. Therefore the pits form an observable border separating material from different overgrown pyramids. Fig. 14b is a misorientation map that is created by indexing all of the patterns acquired at the surface, then applying a gradient scale to indicate the degree of misorientation from a reference point in the data (in this case, the reference point is the pixel located at the image center. By displaying the misorientation in this way, it is easy to see average variations in the misorientations between the material from different overgrown pyramids. Variations indicate the presence of small-angle grain boundaries. Tests of the angular resolution of the EBSD technique show that misorientations as low as 0.25° can be detected [64]. Preliminary analysis of the data used to create Fig. 14b shows that there are a few regions (with slightly darker contrast) that have an average misorientation of approximately 0.5° with respect to the reference orientation.

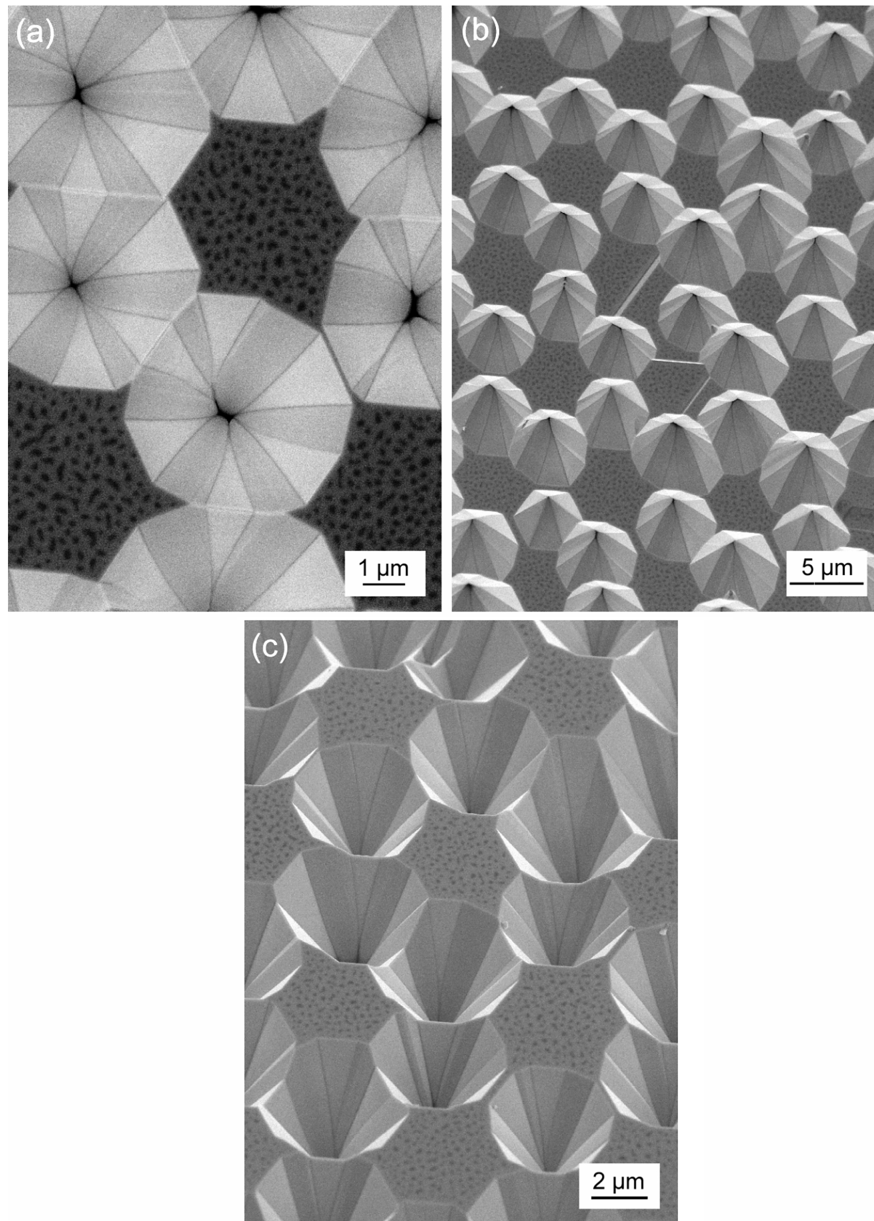

Figure 12 A series of secondary electron images of the surface of GaN after the pyramids have grown together. The images were acquired at various sample tilts. The image in (a) was acquired at 0° tilt. The images in (b) and (c) were tilted with a negative and a positive tilt respectively, to show that the structures are pits and not pyramids.

4. Discussion

The dislocation geometry of the GaN pyramids, as shown in Fig. 1b and c, reveals some important characteristics of the growth process. For example, in the core region a high density of dislocations propagate through the core closely perpendicular to the interface plane. These dislocations then abruptly bend through 90° at or near to the inclined faces at the edge of the pyramid core. This observation suggests that the initial GaN growth (above the mask aperture) and the defect propagation (threading dislocations) took place in the [0001] direction. The subsequent lateral growth of the GaN on the facets results in the horizontal propagation of the dislocations in the outer part of the pyramid, which leads to the elimination of the dislocations in the top part of the pyramid. Thus, the dislocations do not bend by moving, rather they bend by propagating in a different direction [7, 35, 59].

The density of the dislocations in the lateral growth region appears to be reduced from that of bulk GaN ($\sim 10^{10}$ cm^{-2}) [65, 66]. The study of dislocations in this region reveals that many have a Burgers vector of type $\mathbf{b} = 1/3\langle 11\bar{2}0\rangle$ and a line direction of $\langle 11\bar{2}0\rangle$ or $\langle 01\bar{1}0\rangle$. Many of these dislocations are the threading dislocations from the core region that have bent over upon entering

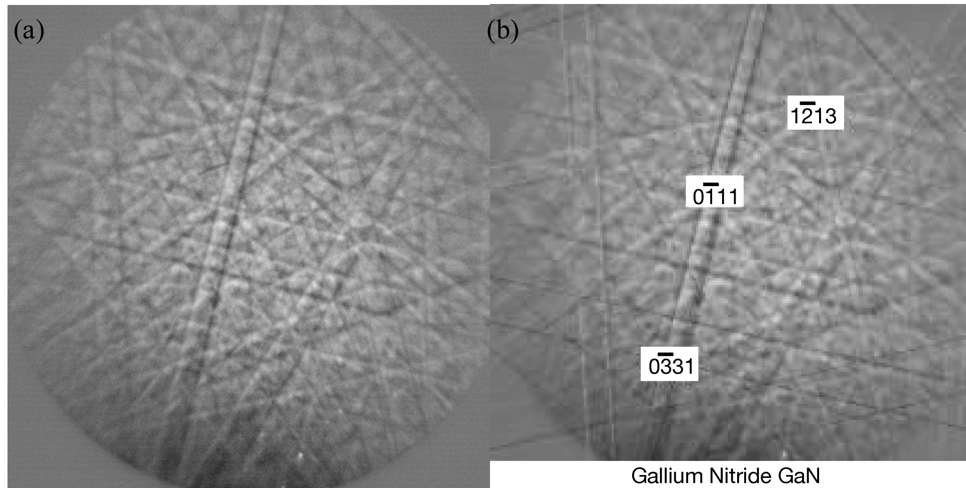

Figure 13 (a) An EBSD pattern from the as-grown surface of GaN. (b) The same pattern after indexing using the structural information for GaN. An indexing overlay is shown on the pattern to illustrate the indexing fit.

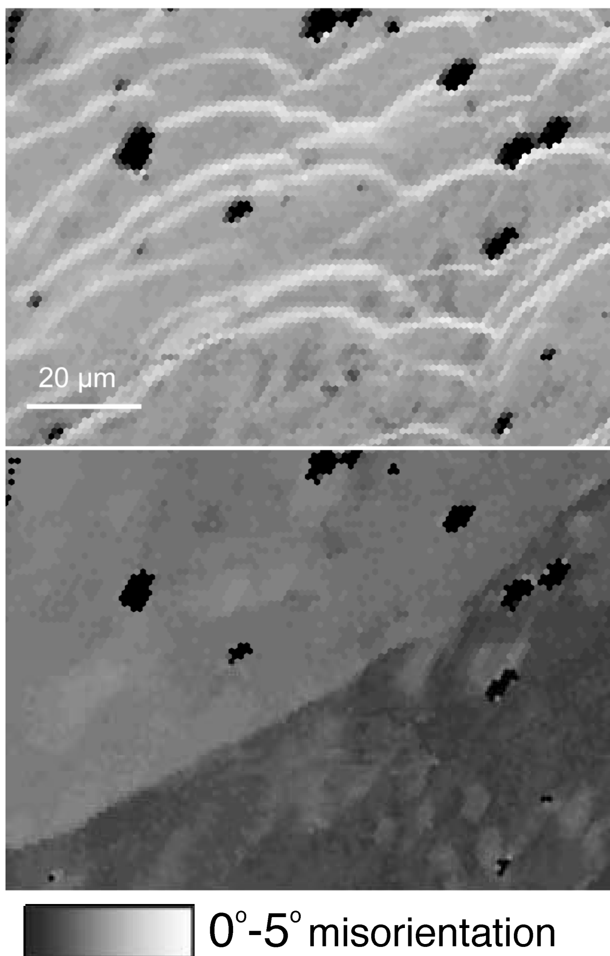

Figure 14 An IQ map (a) and a misorientation map (b) of the surface of the over grown GaN.

the lateral-growth region. This effect was proposed for continuous films grown by LEO [61] and demonstrated for individual pyramids [7, 59]. Therefore the dislocation half loops, which are located in the core region and have a Burgers vector of $\mathbf{b} = [0001]$, are either pure screw or mixed in character as long as they remain in the core region. The threading dislocations, which are found in the core and have a Burgers vector of $\mathbf{b} = 1/3\langle 11\bar{2}0\rangle$, are mostly edge in nature as long as they remain in the core. However as soon as they reach the edge of the core they could potentially become pure edge, pure screw, or mixed in character.

The dislocations found in the GaN pyramids are merely extensions of the dislocations originating in the GaN/AlN buffer layer. Therefore, in order to understand the source of the dislocations in the GaN pyramid, the source of the dislocations must be studied. An analysis similar to that performed by Ning *et al.* [67], for GaN on basal sapphire, was applied to GaN on (111) Si. In studying heteroepitactic films, the lattice mismatch of greatest significance is that of the planes in the epilayer and substrate that are perpendicular to the interface and parallel to each other. Therefore, for GaN grown on (0001) sapphire, the planes that are of main significance for mismatch are the $\{\bar{1}100\}$ planes of GaN and the $\{11\bar{2}0\}$ planes of sapphire; for GaN grown on (111) Si, the significant planes are the $\{11\bar{2}0\}$ planes of GaN and the $\{\bar{2}20\}$ planes of Si. The epilayer/substrate mismatch parameter, $f(\mathrm{T})$, at temperature T, can be defined as:

$$f(T) = \frac{a_e - a_s}{a_s}$$

Here a_e and a_s represent the interplanar spacings of the corresponding planes in the epilayer and substrate. At room temperature, these spacings are [1]

$$a_{\bar{1}100}^{\mathrm{GaN}} = 0.276\,\mathrm{nm},\ a_{11\bar{2}0}^{\mathrm{Sapphire}} = 0.238\,\mathrm{nm}$$

$$a_{11\bar{2}0}^{\mathrm{GaN}} = 0.159\,\mathrm{nm},\ a_{\bar{2}20}^{\mathrm{Si}} = 0.192\,\mathrm{nm}$$

Therefore, the misfit parameter for GaN grown on (0001) sapphire is $f = 0.160 > 0$, and for GaN grown on (111) Si $f = -0.172 < 0$. These values will change slightly with the temperature considering the coefficients of thermal expansion of GaN and sapphire in the basal planes, and the Si in the (111) plane. The corresponding coefficients of thermal expansion are [1]

$$\alpha_{\mathrm{GaN}} = 5.59 \times 10^{-6}/\mathrm{K}$$
$$\alpha_{\mathrm{sapphire}} = 7.5 \times 10^{-6}/\mathrm{K}$$
$$\alpha_{\mathrm{Si}} = 3.59 \times 10^{-6}/\mathrm{K}$$

Although the lattice mismatch for GaN on (111) Si is larger than for GaN on (0001) sapphire, the misfit parameter for GaN on (0001) sapphire is more strongly affected by temperature than that of GaN on (111) Si. Another consideration however, is that the strain introduced by the misfit is different for the different substrates. If the lattice misfit at the growth temperature is fully accommodated, the thermal mismatch dictates that, after cooling to room temperature, the GaN on sapphire will be in compression while GaN on Si will be in tension. The importance of this difference has been described previously for GaAs-based materials [68]. Variations in the dislocation formation during the growth process may be introduced by these differences.

5. Conclusions

GaN pyramids were grown using the LEO technique on GaN/AlN seeding layers through patterned apertures in a Si_3N_4 mask. The seeding layers were grown on (111) Si substrates and based on the selected area diffraction analysis, the following epitactic relationship was found between the GaN pyramid, GaN seed layer, AlN buffer layer, and the Si substrate: $[11\bar{2}0]_{\mathrm{GaN}}||[11\bar{2}0]_{\mathrm{AlN}}||[\bar{1}10]_{\mathrm{Si}}$ and $(0001)_{\mathrm{GaN}}||(0001)_{\mathrm{AlN}}||(111)_{\mathrm{Si}}$.

The GaN pyramids can be described as a core region above the initial aperture in the mask, a lateral growth or outer region with a film thickness the same as the core, and a top region above the core and lateral growth region. The core appears to have the same shape as the pyramid itself. In the core of the pyramids, there is a high density of dislocations propagating through the pyramid perpendicular to the original interface plane. Some of these threading dislocations, which originated from the GaN/AlN seed layer, bend through 90° and emerge on the inclined faces at the edge of the pyramid core. In the lateral growth region of the GaN pyramid, the dislocation density is low relative to that of the core. The majority of dislocations in this region thread through the pyramid parallel to the interface plane. The Burgers vectors of the majority the dislocations in the pyramid were found to be $\mathbf{b} = 1/3\langle 11\bar{2}0\rangle$ and $\mathbf{b} = [0001]$. The defect density decreases with the distance away from the interface, the top several microns of material being essentially defect-free.

Appendix

A.1 Thickness-fringe contrast analysis of defects in GaN

The analysis of thickness-fringe contrast in weak-beam transmission electron microscope (TEM) images has been shown to be a reliable method for the complete determination of the character, as well as the magnitude, of a dislocation Burgers vector. By selecting multiple diffraction conditions and, for each condition, determining the number of terminating thickness fringes at the exit of a dislocation from a wedge-shaped sample, the Burgers vector can be unambiguously determined.

The useful properties of a material are often directly related to the type (i.e. Burgers vector) and density of dislocations present in the material. There are several methods of analyzing dislocation Burgers vectors [1]. One of the most popular of these techniques is based on the "invisibility criterion" ($\mathbf{g} \cdot \mathbf{b} = 0$), which under strong two-beam conditions can determine the direction of the Burgers vector. However, if the dislocation contains a large edge component, the $\mathbf{g} \cdot \mathbf{b} = 0$ condition does not accurately describe the dislocation contrast since there may be a displacement of the lattice that is perpendicular to the Burgers vector (i.e. glide-plane buckling). There are also complications when using a high-order diffracting vector and when the structure of the material is complex.

The thickness-fringe contrast technique overcomes these disadvantages by using the interaction between weak-beam, extinction contours (thickness fringes) and the strain field of a dislocation to analyze the Burgers vector, $\mathbf{b}$ [2]. The behavior of weak-beam extinction contours is sensitive, not only to thickness, but also variations in crystal orientation. It has been shown that the local variations in crystal orientation surrounding a dislocation are manifest by local bending of the extinction contours, and the nature and magnitude of the bending depends on the orientation of the Burgers vector with respect to the diffracting vector of the operating reflector [3]. Therefore, in weak-beam imaging the nature and magnitude of the interaction can be used to determine the sign and magnitude of the Burgers vector of a dislocation.

This technique is based on a two-beam diffraction condition in the TEM. Under these conditions, the Howie–Whelan equations may be used to describe the amplitudes of the transmitted and diffracted beams [4]. Using the "modified" Howie–Whelan equations (modified to account for the presence of a strain field), the following equation can be derived:

$$s_{\mathrm{eff}} = s + \mathbf{g} \cdot \frac{d\mathbf{R}}{dz} \qquad \text{(A1)}$$

where s is the deviation from the exact Bragg condition or excitation error, s_{eff} is the effective excitation error in the presence of a strain field, and $\mathbf{R}$ is the displacement field near a dislocation. The equation describing the behavior of thickness contours, $ts = C$, where t is the local thickness of the sample and C is a constant, can then be modified to

$$ts_{\text{eff}} = t\left[s + \mathbf{g}\cdot\frac{d\mathbf{R}}{dz}\right] = C \qquad \text{(A2)}$$

to account for the presence of a dislocation strain field. Assuming the column approximation is valid [5], consider a column of material near a dislocation. The strain field of the dislocation, $\mathbf{R}$, in the direction, z, of the electron beam creates a gradual change in orientation down the column. Replacing the gradual change in orientation with an average misorientation within the column validates the approximation

$$\left\langle \mathbf{g}\cdot\frac{d\mathbf{R}}{dz}\right\rangle = \frac{\mathbf{g}}{t}\int_0^t \frac{d\mathbf{R}}{dz}dz = \frac{\mathbf{g}}{t}\Delta\mathbf{R} \qquad \text{(A3)}$$

where $\Delta\mathbf{R} = [\mathbf{R}(t) - \mathbf{R}(0)]$. Then substituting equation (3) into (2) yields

$$ts_{\text{eff}} = ts + \mathbf{g}\cdot\Delta\mathbf{R} = C \qquad \text{(A4)}$$

Now if a closed loop L is taken within the material and around the dislocation line, the displacement vector $\Delta\mathbf{R}$, taken along the circuit L in a right-hand sense, is $\Delta\mathbf{R}|_L = \mathbf{b}$. The first term on the right-hand side of the above equation, ts, is zero after integration about the closed circuit. However, the second term $\mathbf{g}\cdot\Delta\mathbf{R}|_L = \mathbf{g}\cdot\mathbf{b}$ is only zero if $\mathbf{g}$ and $\mathbf{b}$ are perpendicular. The left-hand side of Equation (4) taken around the circuit L is $ts_{\text{eff}}|_L = n$, which is the difference in the number of fringes that exit and the number that enter the closed circuit [6]. Therefore, under weak-beam conditions, the number of terminating fringes n at the dislocation is equal to $\mathbf{g}\cdot\mathbf{b}$.

In the above argument, the location of the closed circuit L is not specified except that it is within the material. Therefore the terminating fringes must also be within the material. However, if the location of L is now specified at the bottom surface of the foil as shown in Fig. A.1, the same argument applies, but the fringes are seen in the micrograph where the dislocation intersects the free surface. If the sign of the dislocation in Fig. A.1 is assumed to be positive in the direction toward the specimen edge and the closed loop L is again taken in a right-hand sense around the dislocation, the number of terminating fringes is n. The sign of the Burgers vector can then be determined according to the following: first, assume the end of the specimen foil is toward the bottom of the image (as in Fig. A.1); then, n is positive when n terminating fringes appear in the image on the left-hand side of the dislocation outcrop; and n is negative when n terminating fringes appear on the right-hand side of the dislocation [2].

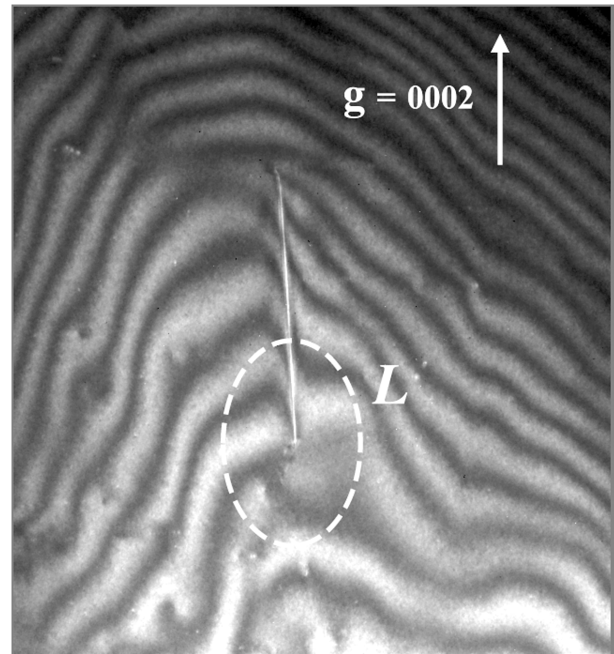

Figure A.1. A low magnification WBDF TEM image of a dislocation. A closed loop L is taken around the dislocation closest to the edge of the specimen foil (toward the bottom of the image).

A2. References

1. D. B. Williams and C. B. Carter. "Transmission Electron Microscopy-A Textbook for Materials Science" (Plenum Press, 1996).
2. Y. Ishida, H. Ishida and K. Kohra. in "Fifth International Conference on High Voltage Electron Microscopy" (Kyoto, 1977) p. 623.
3. F. W. Schapink, *Phys. Status Solidi A* **29** (1975) 623.
4. A. Howie and M. J. Whelan, *Proc. R. Soc. London, Series A, Math. Phys. Sci.* **A263** (1961) 217.
5. P. B. Hirsch, A. Howie and M. J. Whelan, *Phil. Trans. R. Soc. London, Series A, Math. Phys. Sci.* **A252** (1960) 499.
6. Y. Ishida, Ishida, H., Kohra, K., and Ichinose, H. *Phil. Mag. A* **42** (1980) 453.

Acknowledgments

The authors would like to acknowledge many invaluable discussions with Dr Zhigang Mao and Dr Wei Yang who provided the samples. This research has been supported by Honeywell Technology Center and NSF under grant DMR-0102327. The TEM was part of the Characterization Facility at the University of Minnesota. The authors thank Chris Frethem for technical assistance using the Hitachi S-900 SEM.

References

1. S. STRITE and H. MORKOC, *J. Vac. Sci. Tech. B* **10** (1992) 1237.
2. R. F. DAVIS, S. EINFELDT, E. A. PREBLE, A. M. ROSKOWSKI, Z. J. REITMEIER and P. Q. MIRAGLIA, *Acta Mater.* **51** (2003) 5961.
3. A. MILLS, *III-Vs Rev.* **16** (2003) 38.
4. I. MELNGAILIS, *Proc. SPIE* **5123** (2003) 231.
5. Y. LUO, C. SUN, Z. HAO, Y. HAN, B. XIONG, W. GUO and T. WU, in "Proc. 6th Chinese Optoelectronics Symp." (IEEE, Hong Kong, China, 2003) p. 11.
6. O. H. NAM, M. D. BREMSER, B. L. WARD, R. J. NEMANICH and R. F. DAVIS, *Japan. J. Appl. Phys.* **36** (1997) L532.
7. W. YANG, S. A. MCPHERSON, Z. MAO, S. MCKERNAN and C. B. CARTER, *J. Cryst. Growth* **204** (1999) 270.
8. S. NAKAMURA, M. SENOH, S. NAGAHAMA, N. IWASA, T. YAMADA, T. MATSUSHITA, H. KIYOKU, Y. SUGIMOTO, T. KOZAKI, H. UMEMOTO, M. SANO and K. CHOCHO, *Japan. J. Appl. Phys.* **36** (1997) L1568.
9. A. USUI, H. SUNAKAWA, A. SAKAI and A. A. YAMAGUCHI, *ibid.* **36** (1997) L899.
10. C. CHEN, J. YANG, H. WANG, J. ZHANG, V. ADIVARAHAN, M. GAEVSKI, E. KUOKSTIS, Z. GONG, M. SU and M. ASIF KHAN, *Japan. J. Appl. Phys. (Lett.)* **42** (2003) 640.
11. J.-M. BETHOUX, P. VENNEGUES, F. NATALI, E. FELTIN, O. TOTTEREAU, G. NATAF, P. DE MIERRY and F. SEMOND, *J. Appl. Phys.* **94** (2003) 6499.
12. C. H. KO, Y. K. SU, S. J. CHANG, T. Y. TSAI, T. M. KUAN, W. H. LAN, J. C. LIN, W. J. LIN, Y. T. CHERNG and J. B. WEBB, *Mater. Chem. Phys.* **82** (2003) 55.
13. H. NAOI, M. NARUKAWA, H. MIYAKE and K. HIRAMATSU, *J. Cryst. Growth* **248** (2003) 573.
14. F. WANG, R. ZHANG, X. Q. XIU, K. L. CHEN, S. L. GU, B. SHEN, Y. D. ZHENG and T. F. KUECH, *Mater. Lett.* **57** (2003) 1365.
15. E. BAUSER, in "Atomic Mechanism in Semiconductor Liquid Phase Epitaxy," edited by D. T. J. Hurtle, (Elsevier, 1994) Vol. B, p. 879.
16. D. D. RATHMAN, D. J. SILVERSMITH and J. A. BURNS, *J. Electrochem. Soc.* **129** (1982) 2303.
17. T. NISHINAGA, T. NAKANO and S. ZHANG, *Japan. J. Appl. Phys.* **27** (1988) L964.
18. B. Y. TSAUR, R. W. MCCLELLAND, J. C. C. FAN, R. P. GALE, J. P. SALERNO, B. A. VOJAK and C. O. BOZLER, *Appl. Phys. Lett.* **41** (1982) 347.
19. N. H. CHO, C. B. CARTER, Z. ELGAT and D. K. WAGNER, *Appl. Phys. Lett.* **49** (1986) 29.
20. S. NARITSUKA, T. NISHINAGA, M. TACHIKAWA and H. MORI, *Japan. J. Appl. Phys. (Lett.)* **34** (1995) 1432.
21. H. ASAI, S. ADACHI, S. ANDO and K. OE, *J. Appl. Phys.* **55** (1984) 3868.
22. A. G. BHUIYAN, A. HASHIMOTO and A. YAMAMOTO, *ibid.* **94** (2003) 2779.
23. J. BRAULT, S. TANAKA, E. SARIGIANNIDOU, J.-L. ROUVIERE, B. DAUDIN, G. FEUILLET and H. NAKAGAWA, *ibid.* **93** (2003) 3108.
24. L.-W. JI, Y. K. SU, S. J. CHANG, C. S. CHANG, L. W. WU, W. C. LAI, X. L. DU and H. CHEN, *J. Cryst. Growth* **263** (2004) 114.
25. Y. K. SU, S. J. CHANG, L. W. JI, C. S. CHANG, L. W. WU, W. C. LAI, T. H. FANG and K. T. LAM, *Semicond. Sci. Tech.* **19** (2004) 389.
26. T. FUKAI, S. ANDO and Y. K. FUKAI, *Appl. Phys. Lett.* **57** (1990) 1209.
27. H. WANG, C. CHEN, Z. GONG, J. ZHANG, M. GAEVSKI, M. SU, J. YANG and M. A. KHAN, *ibid.* **84** (2004) 499.
28. D. S. LI, H. CHEN, H. B. YU, H. Q. JIA, Q. HUANG and J. M. ZHOU, *J. Cryst. Growth* **267** (2004) 395.
29. F. WU, M. D. CRAVEN, S.-H. LIM and J. S. SPECK, *J. Appl. Phys.* **94** (2003) 942.
30. P. RUTERANA, B. BEAUMONT, P. GIBART and Y. MELNIK, *MRS Internet J. Nitride Semicond. Res.* **5S1** (2000) W2.5.
31. Y. P. HSU, S. J. CHANG, Y. K. SU, J. K. SHEU, C. T. LEE, T. C. WEN, L. W. WU, C. H. KUO, C. S. CHANG and S. C. SHEI, *J. Cryst. Growth* **261** (2004) 466.
32. D. GOGOVA, A. KASIC, H. LARSSON, C. HEMMINGSSON, B. MONEMAR, F. TUOMISTO, K. SAARINEN, L. DOBOS, B. PECZ, P. GIBART and B. BEAUMONT, *J. Appl. Phys.* **96** (2004) 799.
33. B. BEAUMONT and P. GIBART, *Proc. SPIE* **3725** (1999) 2.
34. H. MIYAKE, R. TAKEUCHI, K. HIRAMATSU, H. NAOI, Y. IYECHIKA, T. MAEDA, T. RIEMANN, F. BERTRAM and J. CHRISTEN, *Phys. Stat. Sol. (a)* **194** (2002) 545.
35. A. E. ROMANOV, P. FINI and J. S. SPECK, *J. Appl. Phys.* **93** (2003) 106.
36. X. H. WU, P. FINI, E. J. TARSA, B. HEYING, S. KELLER, U. K. MUSHRA, S. P. DENBAARS and J. S. SPECK, *J. Cryst. Growth* **189/190** (1998) 231.
37. J. K. FARRER and C. B. CARTER, *Mat. Res. Soc. Symp. Proc. (Spring 2001)* **673** (2001) P3.12.
38. S. TANAKA, Y. HONDA, N. KAMESHIRO, R. IWASAKI, N. SAWAKI, T. TANJI and M. ICHIHASHI, *J. Cryst. Growth* **260** (2004) 360.
39. W. JU, D. A. GULINO and R. HIGGINS, *ibid.* **263** (2004) 30.
40. E. FELTIN, B. BEAUMONT, P. VENNEGUES, M. VAILLE, P. GIBART, T. RIEMANN, J. CHRISTEN, L. DOBOS and B. PECZ, *J. Appl. Phys.* **93** (2003) 182.
41. S. HAFFOUZ, A. GRZEGORCZYK, P. R. HAGEMAN, P. VENNEGUES, E. W. J. M. VAN DER DRIFT and P. K. LARSEN, *J. Cryst. Growth* **248** (2003) 568.
42. A. DADGAR, M. POSCHENRIEDER, J. BLASING, O. CONTRERAS, F. BERTRAM, T. RIEMANN, A. REIHER, M. KUNZE, I. DAUMILLER, A. KRTSCHIL, A. DIEZ, A. KALUZA, A. MODLICH, M. KAMP, J. CHRISTEN, F. A. PONCE, E. KOHN and A. KROST, *ibid.* **248** (2003) 556.
43. S. BIDNYK, B. D. LITTLE, Y. H. CHO, J. KRASINSKI, J. J. SONG, W. YANG and S. A. MCPHERSON, *MRS Internet J. Nitride Semicond. Res.* **4S1** (1999).
44. Z. MAO, MCKERNAN, C. B., CARTER, W. YANG and S. A. MCPHERSON, *MRS Internet J. of Nitride Semicond. Res. 4S1, G3.13* (1999).
45. Z. MAO, M. T. JOHNSON and C. B. CARTER, *Microsc. Microanal.* **4** (1998) 628.
46. Z. MAO, S. MCKERNAN, C. B. CARTER, Y. W. and S. A. MCPHERSON, *ibid.* **5** (1999) 734.
47. O.-H. NAM, T. S. ZHELEVA, M. D. BREMSER and R. F. DAVIS, *J. Electronic Mater.* **27** (1998) 233.
48. B. MORAN, F. WU, A. E. ROMANOV, U. K. MISHRA, S. P. DENBAARS and J. S. SPECK, *J. Cryst. Growth* **273** (2004) 38.
49. S. NAKAMURA, *Japan. J. Appl. Phys.* **30** (1991) L1705.
50. S. YOSHIDA, S. MISAWA and S. GONDA, *J. Vac. Sci. Tech. B* **1** (1983) 250.
51. I. AKASAKI, H. AMANO, Y. KOIDE, K. HIRAMATSU and N. SAWAKI, *J. Cryst. Growth* **98** (1989) 209.
52. Y. OHBA and S. IIDA, *Japan. J. Appl. Phys. (Lett.)* **41** (2002) 615.
53. N. N. MORGAN, Y. ZHIZHEN and X. YABOU, *Mater. Sci. Eng. B* **B90** (2002) 201.
54. S. BIDNYK, B. D. LITTLE, Y. H. CHO, J. KRASINSKI, J. J. SONG, W. YANG and S. A. MCPHERSON, *Appl. Phys. Lett.* **73** (1998) 2242.

55. Y. ISHIDA, H. ISHIDA, K. KOHRA and H. ICHINOSE, *Phil. Mag. A* **42** (1980) 453.
56. D. B. WILLIAMS and C. B. CARTER, in "Transmission Electron Microscopy: A Textbook for Materials Science" (Plenum, 1996).
57. T. S. ZHELEVA, O.-H. NAM, M. D. BREMSER and R. F. DAVIS, *Appl. Phys. Lett.* **71** (1997) 2472.
58. R. D. UNDERWOOD, D. KAPOLNEK, B. P. KELLER, S. KELLER, S. P. DENBAARS and U. K. MISHRA, *Solid State Electron.* **41** (1997) 243.
59. M. T. JOHNSON, Z. MAO and C. B. CARTER, *Mat. Res. Soc. Symp. Proc. (Fall 1997)* **482** (1997) 405.
60. W. QIAN, M. SKOWRONSKI, M. D. GRAEF, K. DOVERSPIKE, L. B. ROWLAND and D. K. GASKILL, *Appl. Phys. Lett.* **66** (1995) 1252.
61. A. SAKAI, H. SUNAKAWA and A. USUI, *ibid.* **71** (1997) 2259.
62. X. W. WU, L. M. BROWN, D. KAPOLNEK, S. KELLER, B. KELLER, S. P. DENBAARS and J. S. SPECK, *ibid.* **80** (1996) 3228.
63. J. P. HIRTH, and J. LOTHE, in "Theory of Dislocations" (McGraw-Hill Book Company, 1968).
64. M. M. NOWELL, S. I. WRIGHT and B. W. TRUE, in "SCANNING," edited by R. P. Becker, (Washington D.C., 2004) p. 73.
65. S. D. LESTER, F. A. PONCE, M. G. CRAFORD and D. A. STEIGERWALD, *Appl. Phys. Lett.* **66** (1995) 1249.
66. H. MARCHAND, J. P. IBBETSON, P. T. FINI, S. KELLER, S. P. DENBAARS, J. S. SPECK and U. K. MISHRA, *J. Cryst. Growth* **195** (1998) 328.
67. X. J. NING, F. R. CHIEN, P. PIROUZ, J. W. YANG and M. A. KHAN, *J. Mater. Res.* **11** (1996) 580.
68. B. C. DE COOMAN and C. B. CARTER, *Acta Met.* **37** (1989) 2765.